Author(s): Kim, Jang-Yong & Yao, Lide & van Dijken, Sebastiaan

Title: Coherent piezoelectric strain transfer to thick epitaxial ferromagnetic films with large lattice mismatch

Year: 2013

Version: Post print

Please cite the original version:

Kim, Jang-Yong & Yao, Lide & van Dijken, Sebastiaan. 2013. Coherent piezoelectric strain transfer to thick epitaxial ferromagnetic films with large lattice mismatch. Journal of Physics: Condensed Matter. Volume 25, Issue 8. 082205/1-7. ISSN 0953-8984 (printed). DOI: 10.1088/0953-8984/25/8/082205

Coherent Piezoelectric Strain Transfer to Epitaxial Ferromagnetic Films with Large Lattice Mismatch

Jang-Yong Kim, Lide Yao, and Sebastiaan van Dijken*

NanoSpin, Department of Applied Physics, Aalto University School of Science, P.O. Box 15100, FI-00076 Aalto, Finland

*E-mail: sebastiaan.van.dijken@aalto.fi

Abstract

Strain control of epitaxial films using piezoelectric substrates has recently gained significant scientific interest. Despite its potential as a powerful test bed for strain-related physical phenomena and strain-driven electronic, magnetic, and optical technologies, detailed studies on the efficiency and uniformity of piezoelectric strain transfer are scarce. Here we demonstrate that full and uniform piezoelectric strain transfer to epitaxial films is not limited to systems with small lattice mismatch or limited film thickness. Detailed transmission electron microscopy (TEM) and x-ray diffraction (XRD) measurements of 100 nm thick $CoFe_2O_4$ and $La_{2/3}Sr_{1/3}MnO_3$ epitaxial films on piezoelectric $0.72Pb(Mg_{1/3}Nb_{2/3})O_3$-$0.28PbTiO_3$ substrates (+4.3% and −3.8% lattice mismatch) indicate that misfit dislocations near the interface do not hamper the transfer of piezoelectric strain. Instead, the epitaxial magnetic oxide films and PMN-PT substrates are strained coherently and their lattice parameters change linearly as a function of applied electric field when their remnant growth-induced strain state is negligible. As a result, ferromagnetic properties such as the coercive field, saturation magnetization, and Curie temperature can reversibly be tuned by electrical means. The observation of efficient piezoelectric strain transfer in large-mismatch heteroepitaxial structures opens up new routes towards the engineering of strain-controlled physical properties in a broad class of hybrid material systems.

Tailoring of material properties by strained epitaxy is intensively used as a tool in fundamental studies and practical devices. A multitude of examples exist. For example, in ferroelectric and ferromagnetic films, strain states are utilized to control ferroic order parameters, phase transitions, and domain configurations [1-5]. Strain manipulation of the carrier mobility in semiconductors has led to the application of biaxially strained channels in metal-oxide-semiconductor field-effect transistors [6,7]. Moreover, strain-relaxation processes form the basis for the fabrication of various self-organized nanostructures [8,9]. Conventionally, strain engineering in epitaxial systems is pursued by appropriate selection of film and substrate material. Differences in lattice parameter or crystal symmetry result in the accumulation of strain energy during film growth. For large lattice mismatch $f = (a_f - a_s)/a_s$, where a_f and a_s are the in-plane lattice parameters of film and substrate, the strain energy builds up rapidly. As a result, strain relief via the formation of misfit dislocations and/or a transition to three-dimensional island growth occurs, leading to non-uniform strain distributions along the growth direction. According to the thermodynamic model by Matthews and Blakeslee [10,11], 100 nm thick epitaxial films can only be strained uniformly if $|f| < 0.2\%$. Besides misfit strain, epitaxial films also acquire thermal strain during cool down from elevated deposition temperatures if the thermal expansion coefficients of the film and substrate differ. The total thermal strain is limited by strain relaxation mechanisms such as dislocation glide or grain boundary diffusion, which are often detrimental to the performance of thin-film devices that are operated far away from their fabrication temperature. Both lattice misfit strain and thermal strain are fixed after film growth and thus cannot be altered during device operation.

For studies on the evolution of material properties under reversible strain conditions, thin films have been successfully grown onto piezoelectric substrates. The most commonly used piezoelectric substrate is $(1\text{-}x)Pb(Mg_{1/3}Nb_{2/3})O_3\text{-}xPbTiO_3$, which is a well-known relaxor ferroelectric material with excellent electromechanical and piezoelectric properties for compositions near the morphotropic phase

boundary ($0.25 \leq x \leq 0.35$) [12]. Piezoelectric strain transfer from PMN-PT substrates has, for example, been used to tune the magnetic properties of manganite [13,14], ferrite [15-19], and metallic magnetic films [20-23], to alter the electrical resistance of magnetic oxides [13,18,24-26], to demonstrate strain-controlled light emission from semiconductor heterostructures [27,28], and to tailor the properties of graphene [29]. In addition, strain-modulation of magnetic properties on a microscopic scale has recently been demonstrated in ferromagnetic-ferroelectric hybrids [30-32], which has opened new ways to electric control of ferromagnetic domain formation and magnetic domain wall motion [33,34]. While reversible strain actuation by an applied electric field has been used as a powerful tool to actively tailor hybrid material systems, possible limitations due to strain relaxation and defect formation during thin film growth are still largely unexplored. In this Communication, we use TEM and XRD to analyze the correlation between growth-induced strain states and the ability to actively alter material properties using piezoelectric strain. We compare two archetypical ferromagnetic oxide film/piezoelectric substrate combinations, namely $CoFe_2O_4$ (CFO) and $La_{2/3}Sr_{1/3}MnO_3$ (LSMO) on $0.72Pb(Mg_{1/3}Nb_{2/3})O_3$-$0.28PbTiO_3$ (PMN-PT).

Insulating CFO is a hard magnetic material with a high degree of magnetic anisotropy and a coercive field of several tenths of Tesla. The magnetic properties of CFO can be understood from its electronic and structural configuration in which the divalent cobalt cations are located on the octahedral sites and the trivalent iron cations are located on the tetrahedral and remaining octahedral sites (inverse spinel structure). The unit cell of CFO has a face-centered cubic structure with a lattice parameter of a_{CFO} = 8.39 Å. The Curie temperature of CFO is ~790 K. The mixed valence manganite LSMO has been intensively studied because it exhibits colossal magnetoresistance [35]. The Curie temperature of bulk LSMO is ~370 K. LSMO possesses a rhombohedral structure at room temperature with a corresponding pseudo-cubic lattice parameter of a_{LSMO} = 3.870 Å and an angle between the axes of α =

89.74°. Finally, PMN-PT crystals with 28% $PbTiO_3$ content are monoclinic after poling with a pseudo-cubic lattice parameter of $a_{PMN\text{-}PT}$ = 4.021 Å and an angle between the [100] and [010] planes of α = 89.92° [36]. The lattice mismatch between CFO and PMN-PT is $f = (0.5a_{CFO} - a_{PMN\text{-}PT})/a_{PMN\text{-}PT}$ = +4.3% and that of LSMO and PMN-PT equals –3.8%.

The CFO and LSMO films were grown on (001)-oriented $0.72Pb(Mg_{1/3}Nb_{2/3})O_3$-$0.28PbTiO_3$ single crystal substrates using pulsed laser deposition (PLD). The base pressure in the deposition chamber was 10^{-8} mbar. The fluence of the 25 ns laser pulses (produced with a 248 nm KrF excimer laser from *Lambda Physik*) was 2.5 J/cm^2 and the pulse repetition rate was set to 4 Hz. The CFO films were deposited at 650°C in an oxygen pressure of 0.1 mbar. The LSMO films were grown in an oxygen atmosphere of 0.5 mbar at a temperature of 800°C. Under these conditions, the deposition rates were about 3 nm/min and 7 nm/min for CFO and LSMO, respectively. The LSMO films were post-annealed at the deposition temperature for 15 minutes in 0.65 mbar oxygen. The thickness of the films was 100 nm. Cross-sectional transmission electron microscopy (TEM) specimens were prepared by conventional methods, i.e. face-to-face gluing of films, subsequent cutting into thin slices, followed by mechanical polishing, dimpling and ion milling. The high-resolution structural observations were carried out on a JEOL 2200FS TEM with double Cs correctors. Different specimens were prepared for imaging along the [100] and [110] zone axes. A FRWRtools plugin for Gatan Digital Micrograph software was used to perform geometric phase analyses (GPA) [37]. The in-plane (ε_{xx}) and out-of-plane (ε_{yy}) strain maps were calculated from HRTEM images using the undisturbed PMN-PT lattice as reference. The evolution of the in-plane and out-of-plane lattice parameters of the CFO and LSMO films as a function of piezoelectric strain was analyzed with a x-ray diffractometer (*PANalytical X'Pert Pro*) using Cu *K*α radiation (λ = 1.54056Å). For these experiments, a large 50 nm Au/5 nm Ti top electrode was deposited onto the surface of the magnetic oxide films and Ag paste on the backside of

the PMN-PT substrates was used as bottom electrode. During the measurements, the out-of-plane electrical field across the 0.5 mm thick PMN-PT substrate was slowly ramped up to E = 12 kV/cm. The out-of-plane c lattice parameters were determined from $\theta - 2\theta$ scans while the pseudo-cubic a lattice parameters were evaluated from reciprocal space maps of the PMN-PT (202), CFO (404), and LSMO (202) reflections. The magnetic properties in an applied electric field were characterized using a superconducting quantum interference device (SQUID) magnetometer (*Quantum Design, MPMS-XL7*). The external electric field was applied to an especially designed sample holder for the DC transport option. The linear diamagnetic PMN-PT and sample holder contributions were subtracted from the measurement data.

Figure 1 shows cross-sectional scanning TEM (STEM) and high-resolution TEM (HRTEM) images of CFO/PMN-PT samples. Electron diffraction patterns from selected interface areas (inset of figure 1(e)) contain two sets of reflections, clearly demonstrating epitaxial cube-on-cube film growth despite the large lattice mismatch. The epitaxial relationships between film and substrate are CFO (001) ‖ PMN-PT (001) and CFO [100] ‖ PMN-PT [100]. The interface structure was analyzed using atomic Z-contrast in cross-sectional high-resolution STEM images (figure 1(c)). In the inverse spinel CFO structure, the divalent cations (Co^{2+}) occupy the octahedral sites, while the trivalent cations (Fe^{3+}) are equally divided among the tetrahedral sites and the remaining octahedral sites. The projection of this atomic structure along the [110] zone axis is schematically illustrated in figure 1(d). A comparison of the CFO lattice structure with the atomic column contrast in the STEM image clearly reveals that a Co/Fe-O plane contacts the Pb-O terminated substrate. The large lattice mismatch between CFO and PMN-PT is relaxed via misfit dislocations at the interface. This is most clearly seen in the Fourier filtered image of figure 1(b). The average distance between misfit dislocations is about 4 nm. This agrees well with theoretical estimations of the dislocation network period along the [110] direction (Λ

$\approx 0.25\sqrt{2}(0.5a_{CFO})a_{PMN\text{-}PT}/(0.5a_{CFO} - a_{PMN\text{-}PT}) = 3.4$ nm), which clearly indicates that most of the lattice strain is accommodated by the formation of a regular dislocation network at the CFO/PMN-PT interface. Further details on lattice strain relaxation are provided by geometric phase analysis (GPA) of HRTEM images along the [100] direction (figure 1(e) – 1(g)). The in-plane (ε_{xx}) and out-of-plane (ε_{yy}) strain maps were calculated using the undisturbed PMN-PT lattice as reference. Except for the dislocation sites, the in-plane strain map is nearly homogeneous. The in-plane lattice parameter of the CFO film relaxes to a value that is about 4% larger than that of the PMN-PT substrate at about 1 – 1.5 nm from the interface, in agreement with the lattice of CFO bulk crystals. The out-of-plane strain map shows more pronounced contrast near the interface. Obviously, ε_{yy} exhibits larger dilations and some contractions around the dislocation cores in the CFO film. This is most clearly illustrated by the line profile of the selected area in figure 1(g). At this location, the out-of-plane lattice parameter first increases up to about 1.2 nm from the interface, after which it quickly relaxes back to the CFO bulk value. After the formation of a regular dislocation network, the strain distribution is uniform along the growth direction.

The opposite lattice misfit strain between LSMO and PMN-PT is also relaxed via the formation of dislocations near the interface (figure 2). In this case, epitaxial cube-on-cube growth is obtained with LSMO (001) || PMN-PT (001) and LSMO [100] || PMN-PT [100]. The interface is a bit rougher than that of the CFO/PMN-PT samples, with a Mn-O plane directly contacting the Pb-O terminated substrate in most areas (figure 2(c) and 2(d)). The average distance between the dislocations is 6 nm, which is larger than the theoretically estimated value of $\Lambda \approx 0.25\sqrt{2}a_{LSMO}a_{PMN\text{-}PT}/(a_{PMN\text{-}PT} - a_{LSMO}) = 3.6$ nm. The lower density of dislocations in the LSMO/PMN-PT samples suggests that some residual and non-uniform strain is present in the LSMO films.

The response of CFO and LSMO films to reversible piezoelectric strain actuation from the PMN-PT substrate was monitored using x-ray diffraction (XRD) in an applied electric field. Figure 3(a) summarizes these experiments. At zero applied electric field, the CFO film is fully relaxed as illustrated by the position of the CFO (004) reflection at the corresponding 2θ angle of its bulk crystal, which agrees with the TEM data. In an out-of-plane electric field, the PMN-PT (002) reflection shifts to lower diffraction angles indicating an elongation of the out-of-plane $c_{PMN\text{-}PT}$ lattice parameter. The maximum piezoelectric strain amounts 0.39% for E = 12 kV/cm. The concurrent biaxial lattice compression in the substrate plane as derived from reciprocal space mapping is summarized in table 1. Piezoelectric strain transfer from the PMN-PT substrate to the CFO film induces a similar deformation of the CFO crystal lattice. The shift of the CFO (004) reflection to lower diffraction angles with increasing electric field corresponds to a linear increase of the c_{CFO} lattice parameter, which closely resembles the E-field dependence of $c_{PMN\text{-}PT}$ (inset of figure 3(a)). The evolution of the in-plane lattice parameter of the CFO film and PMN-PT substrate with applied electric field also closely agree confirming coherent and full piezoelectric strain transfer despite the presence of a dense dislocation network at the CFO/PMN-PT interface. Using the parameters from table 1, the elastic response as described by the Poisson number ($\nu = \delta\varepsilon_{yy}/(\delta\varepsilon_{yy} - 2\delta\varepsilon_{xx})$) can be estimated. We find, $\nu_{PMN\text{-}PT} = 0.23$ and $\nu_{CFO} = 0.22$.

A qualitative similar E-field behavior is observed for LSMO films on PMN-PT. In this case, the tensile in-plane strain that originates from the –3.8% lattice mismatch between LSMO and PMN-PT is not fully relaxed by the misfit dislocation network. The remnant growth-induced strain, as estimated from the upward shift of the zero-field LSMO (002) reflection with respect to the LSMO bulk diffraction angle, amounts 0.4%. We note that this is an average strain value. Based on strain relaxation models it is likely that the LSMO lattice strain is substantially larger just above the dislocation network

and that it gradually decreases towards the top of the film. This scenario is also supported by TEM measurements indicating an insufficient number of lattice dislocations near the interface to fully relax the lattice misfit strain. The growth-induced strain state is altered by the application of an out-of-plane electric field across the PMN-PT substrate. Again, concurrent linear evolutions of $c_{PMN\text{-}PT}$ and c_{LSMO} are measured as a function of E. However, the slope of the out-of-plane piezoelectric strain ($\delta\varepsilon_{yy}$) versus electric field curves (inset of figure 3(b)) is smaller for the LSMO film than the PMN-PT substrate. A similar difference in the electric-field dependence of the in-plane $a_{PMN\text{-}PT}$ and a_{LSMO} parameters is also observed (table 1), indicating that only a part of the piezoelectric strain (about 70%) is transferred to the LSMO film. This incoherent strain relation is most likely caused by the presence of a non-uniform strain distribution after growth, a finding that might be more general for epitaxial systems with substantial strain disorder. Based on the measured lattice parameters listed in table 1, a Poisson number of $\nu_{LSMO} = 0.22$ is estimated for 100 nm thick LSMO films.

Piezoelectric strain alters the magnetic properties of the CFO and LSMO films. In the CFO films, the compressive in-plane strain that is transferred from the PMN-PT substrate induces a magnetoelastic anisotropy energy (K_{me}) via inverse magnetostriction. In the plane of the CFO film, $K_{me}(E) = -3\sigma(E)\lambda/2$, where σ is the in-plane stress and λ is the magnetostriction coefficient (-6.7×10^{-4} [38]). Since both σ and λ are negative, the in-plane magnetoelastic anisotropy energy decreases in an applied electric field and, consequently, a more in-plane alignment of the CFO film magnetization is favored. The experimental data in figure 4 confirm this. The in-plane magnetic hysteresis curves show that the remnant magnetization increases by 32% in an electric field of 10 kV/cm. The evolution of the remnant magnetization and coercivity with electric field are approximately linear (inset of figure 4), which also suggests that both parameters depend linearly on piezoelectric strain ($\delta\varepsilon_{xx}$). To put the electric-field effects in perspective, we estimated the value of K_{me} from the experimental data. Using σ

= $\delta\varepsilon_{xx}Y$, where Y is Young's modulus of CFO (1.4×10^{11} J/m^3 [37]), we find K_{me} (10 kV/cm) = 7.3×10^5 J/m^3. Although this electric-field induced magnetoelastic anisotropy is significant, it is still small compared to the magnetocrystalline anisotropy of CFO (2.6×10^6 J/m^3 [39]). Electric-field induced 90° magnetic switching events, which have been observed in strain-based systems with softer ferromagnetic materials [30-33], are therefore not obtained in CFO/PMN-PT.

The electric-field response of a 100 nm thick LSMO film is summarized in figure 5. The data shows that piezoelectric strain from the PMN-PT substrate changes the saturation magnetization, the magnetic anisotropy, and the Curie temperature of the mixed-valence manganite. The saturation magnetization curves for zero electric field and 8 kV/cm cross each other at a temperature of about 260 K indicating two opposing effects. The in-plane piezoelectric strain increases the Curie temperature of the LSMO film, which results in an electric-field induced enhancement of the saturation magnetization for $T > 260$ K. The increase of the saturation magnetization with applied electric field is approximately linear and hysteretic up to a maximum field of 10 kV/cm (upper right inset of figure 5). At low temperatures, the saturation magnetization decreases in an applied electric field (–2% for $E = 8$ kV/cm at 200°C) and a concurrent change in magnetic anisotropy is measured. The latter effect is clearly illustrated by the shape of the magnetic hysteresis curves in the lower left inset of figure 5. In zero applied electric field, the magnetization curve at 200 K is nearly square, indicating abrupt magnetic switching and full remanence, while the reversal process is more gradual when an electric field of 8 kV/cm is applied across the PMN-PT substrate. The electric field effects in LSMO are partly due to a change of the Mn-O-Mn bond angle and bond lengths under piezoelectric strain conditions. Moreover, it has been reported that lattice strain strongly impacts electron orbital ordering on Mn^{3+} ions in octahedral MnO_6 coordination [40,41].

In summary, coherent piezoelectric strain transfer and electric-field induced anisotropy changes have been achieved in 100 nm thick CFO films on PMN-PT. In this epitaxial system (f = +4.3%), maximum piezoelectric strain effects are facilitated by a dense network of misfit dislocations at the CFO/PMN-PT interface that effectively reduce the growth-induced strain state to zero. In contrast, piezoelectric strain transfer from PMN-PT to epitaxial LSMO films (f = –3.8%) is limited by a non-uniform strain distribution along the growth direction. As electric-field controlled magnetic phenomena based on piezoelectric and ferroelastic strain transfer are currently under intense investigation, it is expected that further studies on the relation between growth dynamics and electric-field induced strain effects will emerge from this work.

J-Y.K. acknowledges support from the Finnish Cultural Foundation. This work was supported by the Academy of Finland (Grant No. 127731).

References

[1] Speck J S, Daykin A C, Seifert A, Romanov A E and Pompe W 1995 *J. Appl. Phys.* **78** 1696

[2] Choi K J, Biegalski M, Li Y L, Sharan A, Schubert J, Uecker R, Reiche P, Chen Y B, Pan X Q, Gopalan V, Chen L-Q, Schlom D G and Eom C B 2004 *Science* **306** 1005

[3] Lee H N, Christen H M, Chisholm M F, Rouleau C M and Lowndes D H 2005 *Nature* **433** 395

[4] Tagantsev A K, Cross L E and Fousek J 2010 *Domains in Ferroic Crystals and Thin Films,* (Springer, New York Dordrecht Heidelberg London)

[5] Hubert A and Schäfer R 1998 *Magnetic Domains: The Analysis of Magnetic Microstructures,* (Springer, Heidelberg, Germany)

[6] Lee M L, Fitzgerald E A, Bulsara M T, Currie M T and Lochtefeld A 2005 *J. Appl. Phys.* ***97*** 011101

[7] Chidambaram P R, Bowen C, Chakravarthi S, Machala C and Wise R 2006 *IEEE Trans. Electron Devices* **53** 944

[8] Teichert C 2002 *Phys. Rep.* **365** 335

[9] Muller P and Saul A 2004 *Surf. Sci. Rep.* **54** 157

[10] Matthews J W and Blakeslee A E 1974 *J. Cryst. Growth* **27** 118

[11] Matthews J W, 1975 *J. Vac. Sci. Technol.* 12 126

[12] Li F, Zhang S, Xu Z, Wei X, Luo J and Shrout T R 2010 *J. Appl. Phys.* **108** 034106

[13] Thiele C, Dörr K, Fähler S, Schultz L, Meyer D C, Levin A A and Paufler P 2005 *Appl. Phys. Lett.* **87** 262502

[14] Thiele C, Dörr K, Bilani O, Rödel J and Schultz L 2007 *Phys. Rev. B* **75** 054408

[15] Yang J J, Zhao Y G, Tian H F, Luo L B, Zhang H Y, He Y J and Luo H S 2009 *Appl. Phys. Lett.* **94** 212504

[16] Park J H, Lee J-H, Kim M G, Jeong Y K, Oak M-A, Jang H M, Choi H J and Scott J F 2010 *Phys. Rev. B* **81** 134401

[17] Park J H, Jeong Y K, Ryu S, Son J Y and Jang H M 2010 *Appl. Phys. Lett.* **96** 192504

[18] Yang Y, Luo Z L, Huang H, Gao Y, Bao J, Li X G, Zhang S, Zhao Y G, Chen X, Pan G and Gao C 2011 *Appl. Phys. Lett.* **98** 153509

[19] Liu M, Obi O, Lou J, Chen Y, Cai Z, Stoute S, Espanol M, Lew M, Situ X, Ziemer K S, Harris V G and Sun N X 2009 *Adv. Funct. Mater.* **19** 1826

[20] Kim J-H, Ryu K-S, Jeong J-W and Shin S-C 2010 *Appl. Phys. Lett.* **97** 252508

[21]Wu T, Bur A, Wong K, Zhao P, Lynch C S, Amiri P K, Wang K L and Carman G P 2011 *Appl. Phys. Lett.* **98** 262504

[22] Hsu C-J, Hockel J L and Carman G P 2012 *Appl. Phys. Lett.* **100** 092902

[23] Lou J, Liu M, Reed D, Ren Y and Sun N X 2009 *Adv. Mater.* **21** 4711

[24] Rata A D, Herklotz A, Nenkov K, Schultz L and Dörr K 2008 *Phys. Rev. Lett.* **100** 076401

[25] Zheng R K, Jiang Y, Wang Y, Chan H L W, Choy C L and Luo H S 2009 *Phys. Rev B* **79** 174420

[26] Wang J, Hu F X, Li R W, Sun J R and Shen B G 2010 *Appl. Phys. Lett.* **96** 052501

[27] Zhang Y, Gao G, Chan H L W, Dai J, Wang Y and Hao J 2012 *Adv. Mater.* **24** 1729

[28] Ding F, Singh R, Plumhof J D, Zander T, Krapek V, Chen Y H, Benyoucef M, Zwiller V, Dörr K, Bester G, Rastelli A and Schmidt O G 2010 *Phys. Rev. Lett.* **104** 067405

[29] Ding F, Li H, Chen Y, Herklotz A, Dörr K, Mei Y, Rastelli A and Schmidt O G 2010 *Nano Lett.* **10** 3453

[30] Lahtinen T H E, Tuomi J O and van Dijken S 2011 *Adv. Mater*. **23** 3187

[31] Lahtinen T H E, Tuomi J O and van Dijken S 2011 *IEEE Trans. Magn.* **47** 3768

[32] Lahtinen T H E, Shirahata Y, Yao L, Franke K J A, Venkataiah G, Taniyama T and van Dijken S 2012 *Appl. Phys. Lett.*. **101** 262405

[33] Lahtinen T H E, Franke K J A and van Dijken S 2012 *Sci. Rep.* **2** 258

[34] Franke K J A, Lahtinen T H E and van Dijken S 2012 *Phys. Rev. B* **85** 094423

[35] Coey J M D, Viret M and von Molnar S 1999 *Adv. Phys.* **48** 167

[36] Biegalski M D, Dörr K, Kim D H and Christen H M 2010 *Appl. Phys. Lett.* **96** 151905

[37] Koch C T, Özdöl V B and van Aken P A 2010 *Appl. Phys. Lett*. **96** 092901

[38] O'Handley A C 2000 *Modern Magnetic Materials: Principles and Applications* (John Wiley & Sons, Inc., New York)

[39] Folen V J 1970 in Landolt-Börnstein *Magnetic and Other Properties of Oxides and Related Compounds* (Springer, Berlin, Heidelberg, New York, vol. 3, part 4b, 366–393)

[40] Qian Q, Tyson T A, Kao C-C, Prellier W, Bai J, Biswas A and Greene R L 2001 *Phys. Rev. B* **63** 224424

[41] Uozu Y, Wakabayashi Y, Ogimoto Y, Takubo N, Tamaru H, Nagaosa N and Miyano K 2006 *Phys. Rev. Lett.* **97** 037202

	PMN-PT			CFO		
	0 kV/cm	10 kV/cm	$\delta\varepsilon$ [%]	0 kV/cm	10 kV/cm	$\delta\varepsilon$ [%]
a [Å]	4.013	3.991	-0.55	8.395	8.351	-0.52
c [Å]	4.024	4.037	0.32	8.386	8.411	0.30

	PMN-PT			LSMO		
	0 kV/cm	10 kV/cm	$\delta\varepsilon$ [%]	0 kV/cm	10 kV/cm	$\delta\varepsilon$ [%]
a [Å]	4.013	4.003	-0.25	3.896	3.889	-0.18
c [Å]	4.024	4.030	0.15	3.855	3.859	0.10

Table 1. Electric-field dependence of the (pseudo-cubic) lattice parameters for CFO (top) and LSMO films (bottom) on PMN-PT. The films are 100 nm thick.

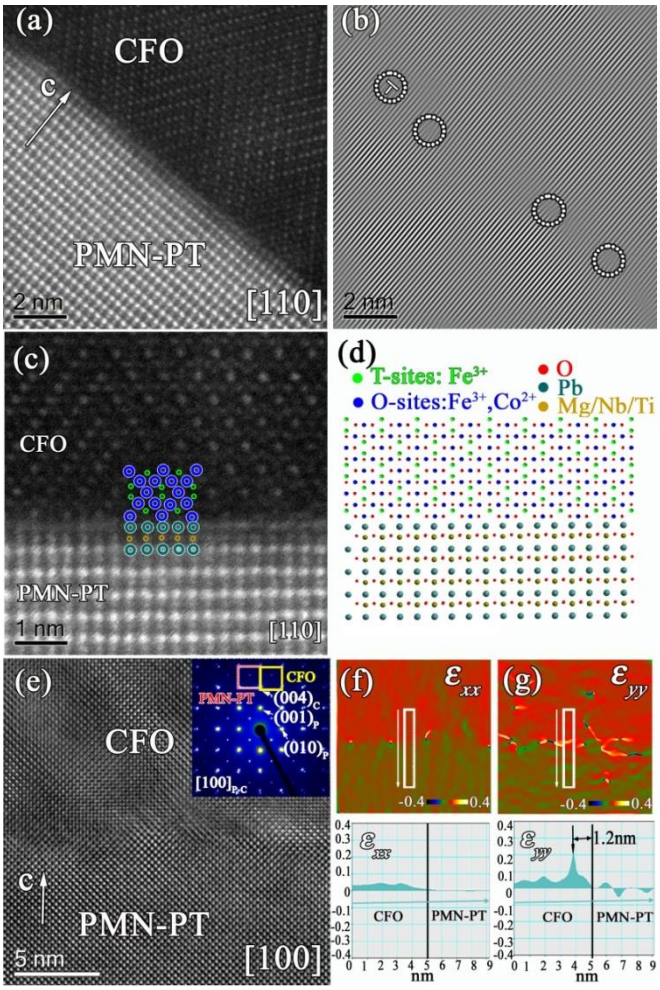

Figure 1. (a) Cross-sectional STEM image of a CFO/PMN-PT sample along the [110] zone axis. (b) (220) Fourier filtered TEM image corresponding to the STEM image in (a) illustrating the formation of dislocations at the interface. (c) STEM image of CFO/PMN-PT and the structural model fit to the atomic arrangement in the interface area. (d) HRTEM image of a CFO/PMN-PT sample along the [100] zone axis. The inset shows an electron diffraction pattern from a selected area containing both the PMN-PT substrate and the CFO film. (e) and (f) In-plane and out-of-plane GPA strain maps. The strain maps are based on the HRTEM image in (d). The lower panels in (e) and (f) show line scans from the selected areas indicated by white boxes.

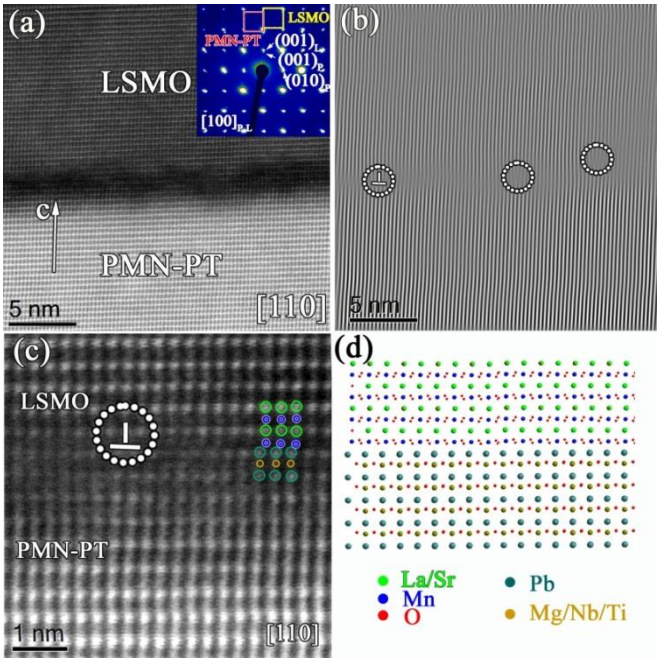

Figure 2. (a) Cross-sectional STEM image of a LSMO/PMN-PT sample along the [110] zone axis. The inset shows an electron diffraction pattern along the [100] zone axis from a selected area containing both the PMN-PT substrate and LSMO film. (b) (220) Fourier filtered TEM image corresponding to the STEM image in (a) illustrating the formation of dislocations at the interface. (c) STEM image of a LSMO/PMN-PT sample and the structural model fit to the atomic arrangements in the interface area.

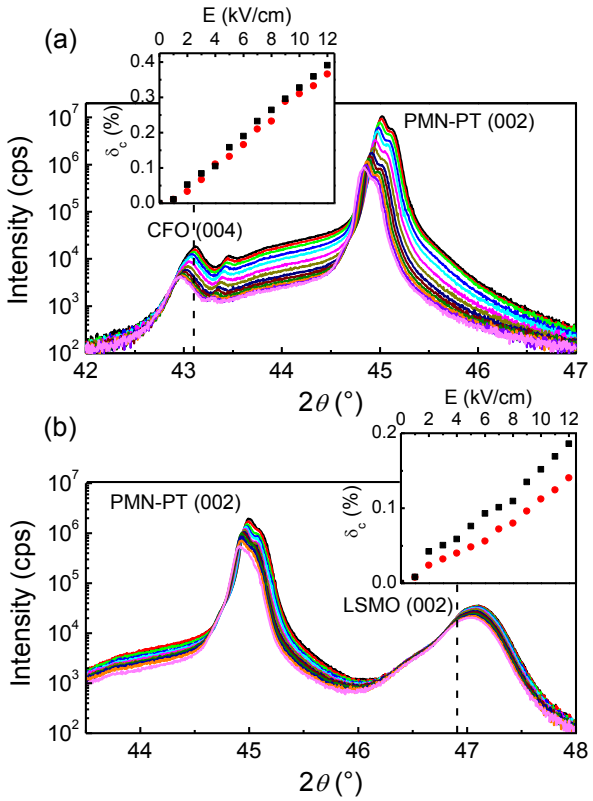

Figure 3. XRD $\theta - 2\theta$ scans for 100 nm thick CFO (a) and LSMO (b) films for different out-of-plane electric fields across the 0.5 mm thick PMN-PT substrate. An increase of the electric field from 0 kV/cm to 12 kV/cm in 1 kV/cm increments shifts the film and substrate reflections to lower diffraction angles. The vertical dashed lines indicate the position of the (004) CFO and (002) LSMO diffraction peaks for bulk lattice parameters. The electric-field induced relative change of the out-of-plane lattice parameters of the PMN-PT substrates (squares) and the CFO and LSMO films (circles) are summarized in the insets.

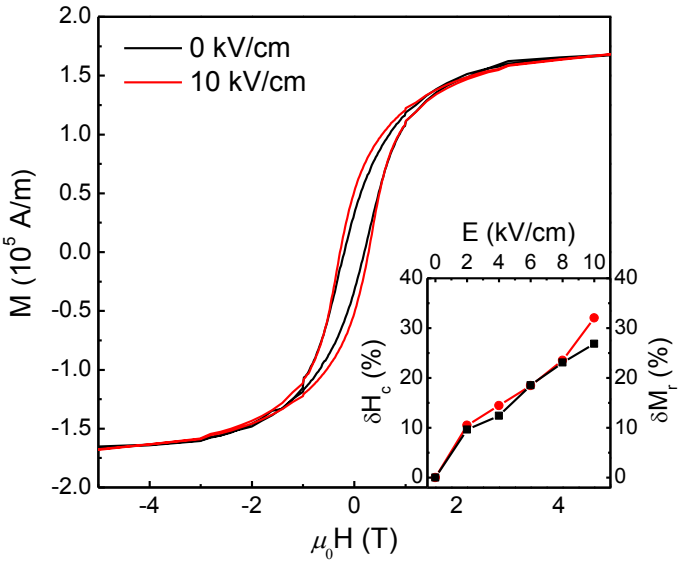

Figure 4. Magnetic hysteresis curves of a 100 nm thick CFO film measured at 300 K with an electric field of 0 kV/cm and 10 kV/cm across the PMN-PT substrate. The inset summarizes the relative change of the coercive field (δH_c, squares) and the remnant magnetization (δM_r, circles) of the CFO film as a function of applied electric field.

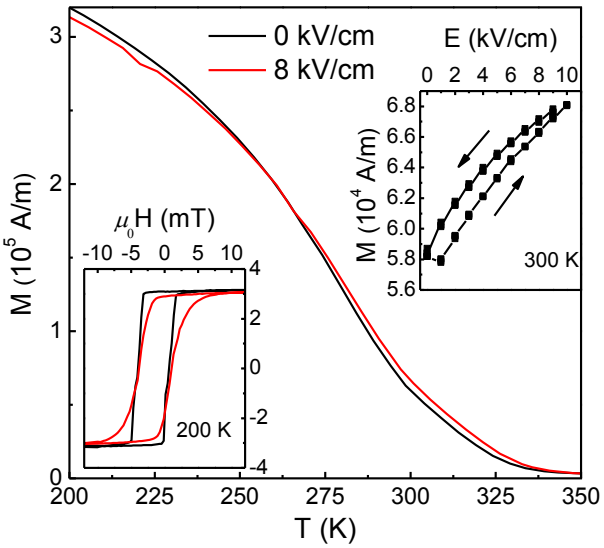

Figure 5. Saturation magnetization of a 100 nm thick LSMO film measured as a function of temperature in a 50 mT magnetic field and an electric field of 0 kV/cm and 8 kV/cm. The lower left inset shows magnetic hysteresis curves for E = 0 kV/cm and E = 8 kV/cm at a temperature of 200 K. The upper right inset summarizes the dependence of the saturation magnetization on applied electric field at 300 K.